

Increasing atmospheric model resolution enhances probability for deep ocean convection

C. Spensberger¹, T. Spengler¹

¹Geophysical Institute, University of Bergen, and Bjerknes Centre for Climate Research, Bergen, Norway

Key Points:

- Higher atmospheric resolution increases probability of deep convection in the ocean
- Overall sensible heat uptake and moisture balance is consistent across resolutions
- Narrower marginal ice zone yields higher peak and overall heat uptake

Corresponding author: Clemens Spensberger, clemens.spensberger@uib.no

Abstract

Modeling air-sea interactions during cold air outbreaks poses a major challenge because of the vast range of scales and physical processes involved. Using the Polar WRF model, we investigate the sensitivity of downstream air mass properties to (a) model resolution, (b) the sharpness of the marginal-ice zone (MIZ), and (c) the geometry of the sea ice edge. The resolved sharpness of the MIZ strongly affects peak heat fluxes and the atmospheric water cycle. For sharper MIZs, roll convection sets in closer to the sea ice edge, increasing both evaporation and precipitation. This yields an increased heat transfer into the atmosphere while the net effect on the atmospheric moisture budget is small. Consequently, higher atmospheric resolution increases the probability that a cold-air outbreak triggers deep convection in the ocean. The geometry of the sea ice edge can induce convergence or divergence zones that affect the air-sea exchange.

Plain Language Summary

In the Arctic, sea-ice insulates a relatively warm ocean from a rather cold atmosphere. From time to time, very cold air masses from over the sea ice spill out over the open ocean. When this happens, large amounts of heat are released from the ocean into the atmosphere, heating the air above while cooling the ocean. Sometimes, the ocean mixed layer becomes dense enough to trigger deep convection contributing to the meridional overturning circulation. In this study, we investigate how simulations of this heat exchange depend on the resolution of the atmospheric model and on properties of the marginal ice zone between pack ice and the open ocean. The higher the resolution of the atmospheric model and the sharper the transition from pack ice to open ocean, the more heat is exchanged between the ocean and the atmosphere. Close to the sea ice edge, the heating also accelerated. Consequently, simulations with higher atmospheric resolution will feature more deep convection in the ocean, which has implications for the strength of the meridional overturning circulation.

1 Introduction

Marine cold air outbreaks (CAOs) constitute a large fraction of the air-sea heat exchange in the polar regions (e.g., Papritz & Spengler, 2017). These atmosphere-ocean interactions are most intense near the sea ice edge and within the Marginal Ice Zone (MIZ), which is also the location where our models and parameterisations are often least accurate (e.g., Bourassa et al., 2013). In addition to challenges with parameterisations, the magnitude and distribution of these air-sea heat exchanges are also sensitive to the representation of mesoscale atmospheric phenomena (e.g., Condrón et al., 2008; Condrón & Renfrew, 2013; Isachsen et al., 2013), the sea ice distribution (Seo & Yang, 2013), and model resolution (e.g., Jung et al., 2014; Haarsma et al., 2016; Moore et al., 2016). To map these sensitivities, we perform a suite of idealised CAO simulations where we vary the model resolution as well as the sea ice concentration within the MIZ.

The MIZ exhibits strong trends in position and width in association with the warming Arctic (Strong, 2012). In this context, our suite of idealised CAO simulations will help to better understand the implications of the warming Arctic for air-sea heat exchange and shed light on potential origins of biases in climate models. For example, changes in sea ice distribution have already been linked to significant changes in the air-sea heat exchange and associated impact on convection in the ocean (Våge et al., 2018). The area around the MIZ is thus of great importance for these exchange mechanisms and feedbacks between the atmosphere, sea ice, and the ocean (Spengler et al., 2016), where the representation of these mechanisms and their intensity can be dependent on model resolution and sea ice distribution.

As models with a resolution typical to global climate models generally fail to reproduce mesoscale atmospheric features and seriously underestimate wind intensity (e.g., Moore et al., 2016), it is important to understand the impact of model resolution on atmosphere-ocean heat exchange. With oceanic convection often driven by episodic strong wind events and CAOs (e.g., Pickart et al., 2003; Våge et al., 2008; Renfrew et al., 2019), investigating these resolution dependencies will also shed light on potential impacts on deep water formation. In the North Atlantic, this formation of dense water is essential for feeding the meridional overturning circulation (e.g., Dickson et al., 1996; Gebbie & Huybers, 2010). It has been shown that a higher atmospheric resolution can lead to either a 5-10% increase in the strength of the Atlantic meridional overturning circulation (AMOC) in an ocean only simulation (Jung et al., 2014) or to a weaker AMOC in fully coupled climate models (Sein et al., 2018). This controversy asks for a more detailed understanding of the resolution dependence of the pertinent processes associated with these air-sea interactions.

In addition, CAOs can be conducive to extreme weather events such as polar lows and polar mesoscale cyclones (e.g., Terpstra et al., 2016; Michel et al., 2018; Stoll et al., 2018). Some of these cyclones can also experience explosive growth leading to extreme latent and sensible heat as well as momentum fluxes (e.g., Inoue & Hori, 2011). Exploring the sensitivity of the evolution of CAOs and their associated air-sea heat exchange with respect to model resolution and sea ice distribution in the MIZ will thus also yield insights into the minimum requirements to adequately predict the essential ingredients giving rise to these phenomena. With the increasing availability of computational resources, model simulations often employ increasingly higher resolutions. How to make the most optimal use of the available resources with respect to model resolution to resolve the pertinent processes, however, remains an open question. Similar to Sein et al. (2018), we thus explore the gain and loss with respect to changes in spatial resolution for the representation of air-sea heat exchange in CAOs in an atmosphere-only setup.

2 Model setup

We base our analysis on a series of idealised model simulations using Polar WRF version 3.9.1 (Hines et al., 2015). We analyze an inner domain of 3072×3072 km with a grid spacing of either 3, 6, 12, 24, 48, or 96 km. This corresponds to a size of the inner domain between 32×32 and 1024×1024 grid points. For all horizontal resolutions, the vertical grid encompasses 60 hybrid model levels with a grid spacing of about 8-10 hPa in the lowest 3 levels and about 25 hPa in the mid-troposphere.

We initialise the domain with horizontally homogeneous winds blowing across an ice edge towards the open ocean. Near-surface wind speeds are initialised with 20 m/s (Fig. 1a), but equilibrate to approximately 12-13 m/s over sea ice and 15-16 m/s over open water due to boundary layer processes. We prescribe a stable temperature profile with 255 K near-surface temperatures and a constant stratification equivalent to a buoyancy oscillation frequency $N^2 = 2.25 \cdot 10^{-4} \text{ s}^{-2}$ (Fig. 1b). Above the tropopause at 6 km height, stratification increases to $N^2 = 4.0 \cdot 10^{-4} \text{ s}^{-2}$ (Fig. 1b). These initial values are prescribed along all lateral boundaries throughout the simulation.

To avoid contamination of the inner domain by the boundary forcing, we pad the inner domain by 8 grid points along all lateral boundaries, resulting in a size of the full domain between 48×48 and 1040×1040 grid points (inner domain: thick gray box, full domain: black box in Fig. 1c). WRF nudges towards the prescribed boundary values in the outermost 5 grid points of the model domain.

In the control setup, we place a straight sharp sea ice edge 480 km downstream of the inflow boundary of the inner domain (pale red rectangle in Fig. 1c). Upstream of the sea ice edge we set the ice concentration to 100%, and skin temperatures to 255 K.

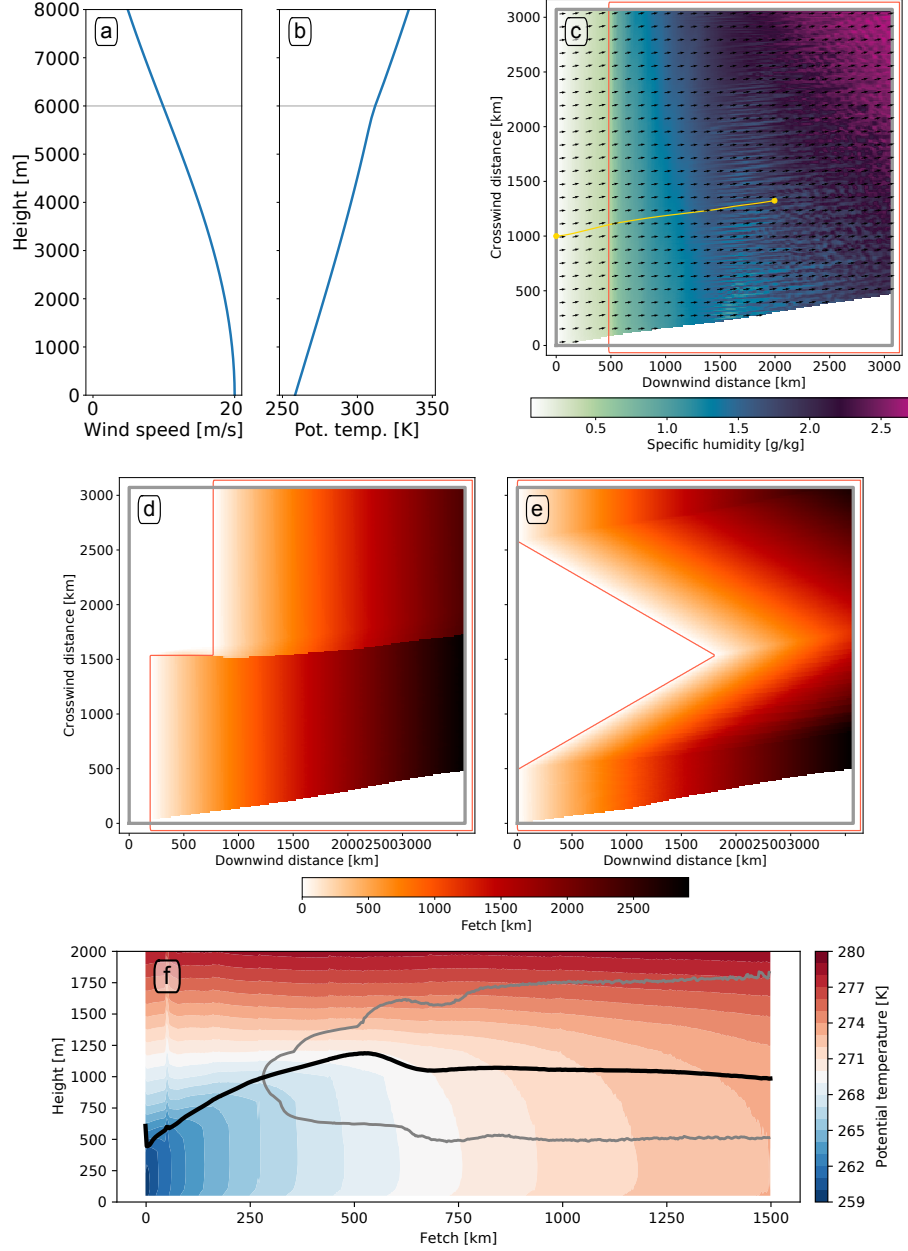


Figure 1. (a,b) Vertical profiles of wind speed and potential temperature used at the initial time and at the upstream boundary around the cross-wind center of the domain. (c) Specific humidity [g/kg] (shading) at 90 h together with wind (arrows) at 300 m above ground level. The yellow line exemplifies a streamline used for the fetch calculation. The pale red contour in (c-e) marks the 50% sea ice concentration, the gray frames indicate the inner domain used for the analyses. Grid points unreachable by horizontal advection from the inflow boundary are masked white and disregarded in the fetch-based analyses. (d,e) Fetch [km] in shading for simulations (d) with a step in the sea ice edge, and (e) a triangular ice edge, both with 12 km grid spacing. The simulations are referred to as S576 and $\Delta 60$, respectively, in sec. 7. (f) Average evolution of potential temperature [K] (shading), boundary layer height (black line), and extent of the cloud layer (gray contour) as a function of fetch for all streamlines in the control simulation with 3 km grid spacing.

Over open water, we set the skin temperature to freezing conditions for typical salt water, 271.3 K. Along the lateral boundaries, we linearly increase the sea-ice concentration from open water to full sea ice cover along the outermost 5 grid points of the full domain (pale red contour in Fig. 1c) to be consistent with the atmospheric forcing at the lateral boundaries that is adapted to sea-ice conditions.

We follow the configuration of the Antarctic Mesoscale Prediction System¹, except for the boundary layer parameterisation. In our tests this parameterisation produced unphysical discontinuities in boundary layer properties, possibly related to changes in the diagnosed boundary layer regime (see supplement for details). We find similar discontinuities with the QNSE scheme (Sukoriansky et al., 2005), but not with the YSU-scheme (Hong et al., 2006), MYNN2.5 and MYNN3 (Nakanishi & Niino, 2006, 2009). As YSU is the default for standard WRF 3.9.1, we decided to use the YSU scheme for our simulations. The MYNN2.5 and MYNN3 schemes yield qualitatively similar results to the YSU scheme (comparison for control setup in supplement).

Besides the boundary layer parametrization, we use the Kain-Fritsch cumulus parametrization for simulations with a grid spacing greater and equal to 12 km (Kain, 2004). At all resolutions, we use the Purdue-Lin microphysics scheme with ice, snow, and graupel processes (Chen & Sun, 2002). We disable radiation and keep skin temperatures constant throughout the simulation. There is thus no diurnal cycle in the surface energy budget.

We integrate the model for 96 hours. The simulated fluxes reach a statistical equilibrium throughout the inner domain by 48 hours of integration. As flow at 20 m/s travels for about 3500 km in 48 hours, the numerical shock associated with slight imbalances in the initial conditions has traveled out of the domain at this point in time. We thus use the final 48 hours of each simulation for our analysis.

3 Comparing simulations based on fetch

We analyze surface fluxes, precipitation and boundary layer properties as a function of fetch d ,

$$d(s) = \int_{s=0}^s (1 - c(s)) ds, \quad (1)$$

the distance traveled over open water. In this equation, $c(s)$ is the local ice concentration, and s is the distance along a streamline (yellow line in Fig. 1c as example), with $s = 0$ at the inflow boundary of the inner domain. Upstream of this inflow boundary, sea ice concentration is kept at 100% for all simulations.

We determine the fetch based on the horizontal time-average flow during the analysis period (48-96 hours) at 300 m above sea level. Using the time-average flow, we calculate streamlines backward from every grid point to trace the flow to the inflow boundary of the inner domain ($x = 0$ in Fig. 1c). Grid points where the streamlines do not trace back to the inflow boundary are discarded. For the control setup, this mask yields the white wedge in the lower right corner of the inner domain (Fig. 1c).

Two example fetch calculations in Fig. 1d,e illustrate the procedure. For a step in the ice edge, the fetch calculation yields a well-defined discontinuity along the convergence zone emerging from the step (Fig. 1d). Further, a slight on-ice flow component across the downwind oriented section of the sea ice edge yields slightly positive fetch values for the first grid points over the sea ice (Fig. 1d). For a triangular ice edge, the fetch field does not feature any discontinuities, but isolines in fetch over open water reflect the triangular geometry of the ice edge (Fig. 1e). As in the control setup, the white wedges

¹ Available online under <https://www2.mmm.ucar.edu/rt/amps/information/configuration/configuration.html>, last accessed 23 April 2020.

in the respective lower right corners in Fig. 1d,e mark regions in which the flow cannot be traced back to the inflow boundary.

As the basic-state flow is geostrophically balanced, surface pressure p_s decreases considerably with increasing crosswind distance. Prescribed temperatures are nearly constant in the cross-wind direction, such that density scales linearly with pressure. The varying surface pressure thus poses a challenge when comparing surface fluxes for the same fetch, because air density affects the magnitude of the air-sea exchange,

$$Q_{sens} = \frac{c_p \rho \kappa^2}{\psi_x^{(10)} \psi_T^{(2)}} U_{10} (\theta_{skin} - \theta_2). \quad (2)$$

Here, the sensible heat flux Q_{sens} is determined by 10-meter wind speed U_{10} and 2-meter potential temperature θ_2 using the stability functions ψ_x and ψ_T for momentum and potential temperature, respectively, evaluated at the height in meters given in parenthesis. κ is the van-Karman constant, c_p the specific heat capacity of moist air at constant pressure, and ρ the air density at the lowest model level.

In summary, $Q_{sens} \propto \rho$ in eq. (2) and $\rho \propto p_s$. To be able to better compare the heat exchange across different cross-wind positions, we thus normalise both sensible and latent heat fluxes to a reference pressure of 1000 hPa,

$$Q_{sens,norm} = \frac{1000 \text{ hPa}}{p_s} Q_{sens}, \quad (3)$$

and analogously for the latent heat flux. With this normalisation, the variability in fluxes across different locations with the same fetch is minimised (shading around the curves in Fig. 2a, b).

4 Control simulation

Our control simulation is based on the control setup with a straight sea ice edge featuring a sharp transition from 100% sea-ice cover upstream to open ocean downstream of the sea ice edge. We use the simulation with 3 km grid spacing as our control simulation with a typical cold air outbreak evolution of the boundary layer (see Fig. 1f).

The initially intense warming declines with increasing fetch. In the boundary layer below the clouds, the isentropes are oriented nearly upright, indicating a well-mixed layer. First clouds form about 250 km downstream of the ice-edge. Except for a step around a fetch of 600 km, the cloud base is nearly horizontal throughout all fetches, suggesting an approximately constant offset between near-surface temperature and dew point.

Both the sensible and the latent heat flux peak slightly downstream of the ice edge (Fig. 2a,b). The respective maxima of about 400 W m^{-2} and 175 W m^{-2} are located at the 4th or 5th grid point of open water. This slight distance between the ice edge and the peak fluxes results from the fluxes depending on both the temperature and moisture contrasts as well as the wind speed. While the temperature and moisture contrasts decrease rapidly due to the fluxes, the wind speed increases from just below 12 m/s over sea ice to just below 16 m/s at a fetch of about 30 km (Fig. 2e).

5 Sensitivity to model resolution

Both the magnitude and the position of the peak sensible heat flux off the ice edge are very consistent between simulations with a grid spacing between 3 km and 24 km (Fig. 2a). Only at 48 km and 96 km the peak sensible heat flux is noticeably lower. However, integrated over the first 96 km of fetch, more heat is extracted in the 96 km simulation than in the 3 km simulation (red curve in Fig. 2c). More generally, lower resolution simulations tend to extract more heat in the first 400 km off the ice edge, but less between

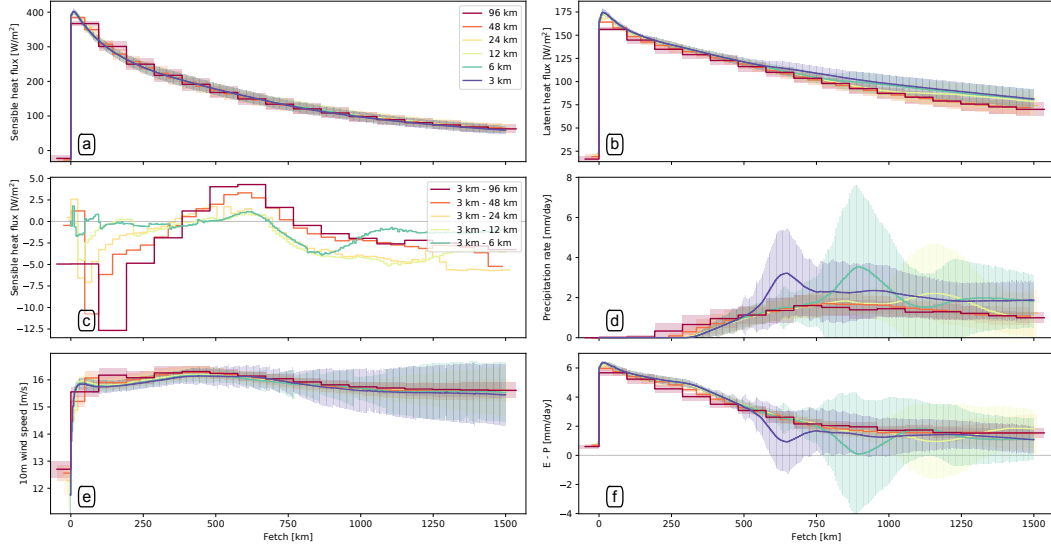


Figure 2. Evolution of the simulated air-sea interaction with fetch. The panels show (a) sensible heat flux (b) latent heat flux, (c) difference in sensible heat flux between resolutions, (d) precipitation rate, (e) 10-meter wind speed U_{10} , and (f) evaporation minus precipitation ($E - P$). Transparent shading around lines indicates the standard deviation amongst all points with the same fetch. Line colors are consistent throughout the panels, except for the difference plot (c).

a fetch of 400 and 700 km. At even larger fetches, slight but systematic differences appear between the simulations with most heat extracted at intermediate resolution (12 and 24 km grid spacing).

The sensible heat fluxes in Fig. 2a are determined by both near-surface temperature contrast and near-surface wind (Eq. 2). Wind speeds are largely consistent across resolutions (Fig. 2e), such that differences in the sensible heat flux are mainly determined by differences in the near-surface temperature contrast (not shown).

In contrast to the sensible heat flux, the latent heat flux is not consistent across resolutions (Fig. 2b). Latent heat fluxes consistently decrease with resolution at all fetches. Consequently, an increase in resolution yields a considerable increase in the total latent heat a simulated cold-air outbreak extracts from the ocean.

For precipitation, the dependence on resolution is even more pronounced (Fig. 2e). A lower resolution results in a precipitation commencing closer to the ice edge. For example, at 96 km grid spacing a slight drizzle occurs already in the second grid cell off the ice edge, whereas precipitation commences at a fetch of about 300 km in the simulation with 3 km grid spacing.

In addition, the structure of precipitation also changes with resolution. At higher resolution, convection starts to organise into linear features with roll convection and cloud streets (cf. Chlond, 1992; Müller et al., 1999). For example, such linear features emerge in the moisture field of the 12 km-simulation in Fig. 1c at a fetch of about 1100 km, coinciding with a slight peak in precipitation (Fig. 2e). At 6 and 3 km grid spacing, roll convection emerges closer to the ice edge (not shown) and yields more pronounced peaks in precipitation (Fig. 2e). The onset of roll convection is thus critically dependent on resolution, with higher resolution yielding earlier onsets. The peak in precipitation shifts considerably from 6 km to 3 km grid spacing, indicating that the atmospheric response has not converged yet at our highest resolution.

At 1500 km fetch the simulations point to two distinct precipitation regimes. The highest resolutions (3 km and 6 km grid spacing) equilibrated at a precipitation rate of approximately 2 mm/day, lower resolutions at about half that value (Fig. 2e). The simulation with 12 km grid spacing does not recover to higher precipitation rates at higher fetches, although roll convection has set in (not shown). This grouping of simulations into precipitation regimes coincides with the grouping by enabled/disabled convection parametrization. This coincidence, however, is by chance. When running our highest resolution cases with convection parametrization enabled, our results do not change.

The different precipitation regimes have only a minor impact on the evaporation minus precipitation moisture budget of the atmosphere ($E-P$; Fig. 2f). At large fetches, all simulations equilibrate at a net moistening of the atmosphere equivalent to about 2 mm of precipitable water per day. The higher rate of precipitation at higher resolution is thus largely offset by higher latent heat fluxes (Fig. 2b), keeping the atmospheric moisture content approximately constant across resolutions, but invigorating the atmospheric water cycle.

In summary, both the sensible heat extraction and the moisture budget is remarkably consistent across resolutions. There are, nevertheless, systematic biases in lower resolution simulations that can affect atmosphere-ocean interactions (cf. Condron & Renfrew, 2013; Jung et al., 2014). First and foremost, the latent heat flux increases with increasing resolution at all fetches. While this increased moisture uptake is offset by increased precipitation, a net heat transport from the ocean to the atmosphere remains together with an increased atmospheric freshwater transport towards larger fetches, which can affect the ocean heat and salinity budgets. In addition, both heat fluxes become more focused close to the sea-ice with increasing resolution.

All these effects act towards destabilizing the water column close to the sea ice edge with increasing atmospheric resolution. Thus, while atmospheric resolution might not significantly alter the downstream evolution of the atmosphere itself, it likely is important for triggering ocean convection.

6 Sensitivity to the sharpness of the marginal ice zone

The sensitivity to model resolution is likely even more pronounced than presented above, as we designed the control setup such that the sea ice edge remains perfectly sharp at all model resolutions. For more realistic setups, the implicit smoothing when interpolating a given sea-ice concentration on a model grid likely exacerbates the effects. We therefore assess the sensitivity of the air-sea heat exchange to combinations of model resolution and the sharpness of the marginal ice zone (MIZ). In addition to the sharp ice edge in the control simulation, we tested transition following a linear profile, (“L50” and “L200”), a tanh-shape (“T50” and “T200”), as well as the negative and positive branches of the tanh-function (“TU50”, “TU200”, and “TL50”, “TL200”, respectively; Fig 3a). For each of the transitions we tested two width with 50 km and 200 km.

Overall, a smoother transition from sea ice to open ocean yields lower peak sensible heat flux (Fig. 3b). In the smoothest profile (T200), the peak flux is reduced by nearly 50% compared to the sharp sea ice edge. In comparison to the sensitivity to the smoothness of the MIZ, peak fluxes are largely consistent across model resolutions, in particular for grid spacings between 3 km and 24 km. Only for the sharpest MIZs is the peak heat flux considerably reduced at the lowest resolutions (cf. 48 and 96 km for the L50 and TU50 simulations in Fig 3b).

For the peak fluxes, it matters where the sharpest gradient in sea-ice concentration occurs within the MIZ. The TL and TU-profiles are symmetric, but differ in whether the sharpest transition occurs either close to the open ocean (TU) or close to sea ice pack (TL). Here, the TL simulations yield markedly lower peak fluxes compared to the TU

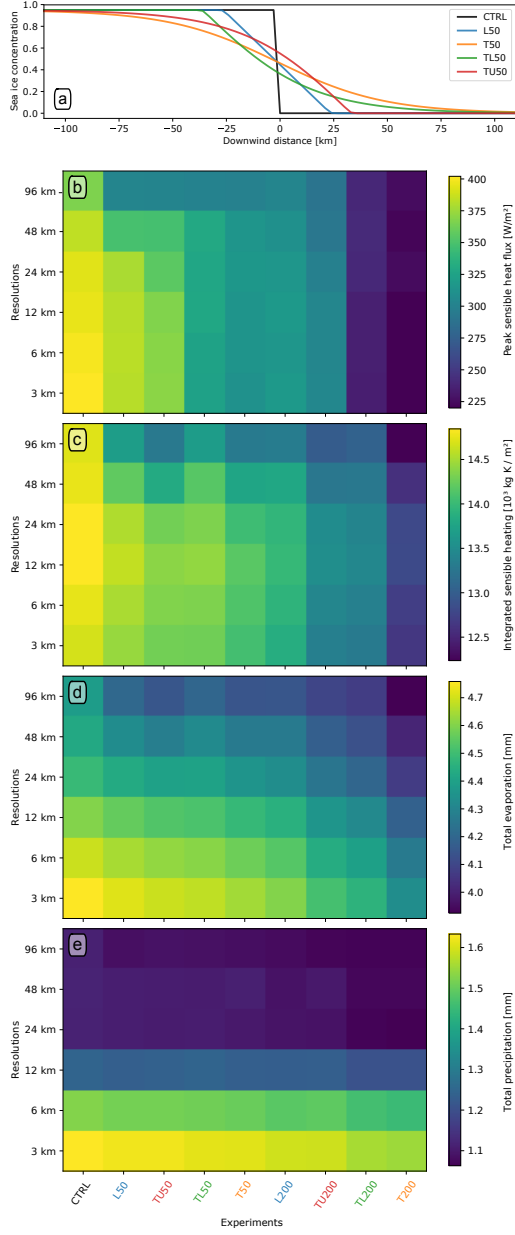


Figure 3. Sensitivity of air-sea heat exchange on both the sharpness of the marginal ice zone and model grid spacing. (a) Profiles of sea ice concentration across the marginal ice zone with a width of 50 km. (b-d) Matrices of (b) peak sensible heat fluxes [W m^{-2}], (c) integrated sensible heating [10^3 kg K m^{-2}], (d) total evaporation [mm], and (e) total precipitation [mm], all up until a fetch of 1500 km. All matrices show the dependence on model grid spacing and the sea ice distribution within the marginal ice zone. The sea ice distribution in the experiments follows the profiles of (a) with width of 50 km and 200 km, respectively.

simulations at both 50 km and 200 km MIZ width scale (Fig. 3b). Hence, it is mainly the sharpness of the MIZ at low sea ice concentrations that determines the peak heat flux.

Integral sensible heat uptake is even less dependent on model resolution than the peak sensible heat flux (Fig. 3b,c). Consistent with the control simulations, integral fluxes for all MIZs are slightly higher at intermediate resolutions (12 km and 24 km grid spacing) compared to both higher and lower-resolution results (Fig. 3c). This effect however is about one order of magnitude smaller than the reduction of integral heat uptake with smoother MIZs. The difference in integral heat uptake between the sharpest and the smoothest transitions amounts to about 20% (Fig. 3c). In contrast to the peak fluxes, the integral heat uptake is nearly identical for the TL and the TU simulations. The integral heat uptake is thus largely insensitive to where the sharpest gradient in ice concentration is located.

Overall, we find a clear dependence of the sensible heat uptake on the sharpness of the MIZ. This result might seem contradictory, given that the sensible heat uptake was largely insensitive to model resolution. These results are, however, not directly comparable, as the reduction in model resolution did not imply an intrinsic smoothing of the MIZ.

In the control simulations, we noted a marked effect of model resolution on the atmospheric water cycle, with both evaporation and precipitation decreasing with resolution. These results for reduced resolution translate only partially to a smoother MIZ. Whereas integral moisture uptake decreases with a smoother MIZ (Fig. 3d), precipitation does not (Fig. 3e). Consequently, a smoother MIZ leads to an overall dryer boundary layer, in particular at larger fetches.

7 Sensitivity to the geometry of the marginal ice zone

In our sensitivity analysis on the sharpness of the MIZ, we kept the sea ice edge as a straight line, oriented perpendicular to the basic state wind. We now proceed to assess the sensitivity of the air-sea heat exchange to the geometry of the MIZ. Specifically, we compare the air-sea exchange for upwind and downwind steps in the sea ice edge as well as convex and concave triangles (Fig. 4). In this analysis we compare grid cells with the same fetch across different simulations, irrespective of where they occur in the model domain. To isolate the effect of the geometry, we prescribe these shapes with a perfectly sharp sea ice edge. Many shapes nevertheless imply partly ice covered grid cells, yielding an implicit smoothing of the sea ice edge with decreasing resolution.

Overall, the geometry of the sea ice edge has only little impact on the peak sensible heat flux (Fig. 4b). To first order, the fluxes depend only on the grid spacing, but not on the shape of the sea ice edge. The implicit smoothing when decreasing the resolution is particularly visible for the 96 km simulations, where the peak fluxes are reduced by 20-25% compared to the CTRL simulation in which the sea-ice edge coincides with a grid cell boundary (Fig. 4b). Exceptions to this rule are the CTRL, S192, S192i and S576i simulations, in which the sea ice edge remains perfectly sharp at each resolution. The S576 simulation constitutes an exception in the peak heat flux at all resolutions, likely because of the slight on-ice flow along the step (cf. discussion of Fig. 1d in sec. 3), which occurs at low fetch values and thus reduces the average heat flux at these fetches.

Similar to the peak heat fluxes, the integrated heat and moisture uptake is largely independent from the geometry of the sea ice edge. Exceptions occur for the narrowest triangles and largest up/downwind steps, featuring pronounced deviations from the straight sea ice edge. In these cases, the sea ice edge induces convergence or divergence lines and thus a degree of mesoscale flow organization. With this organization, the boundary layer evolution along neighboring stream lines is no longer independent. Any such flow organ-

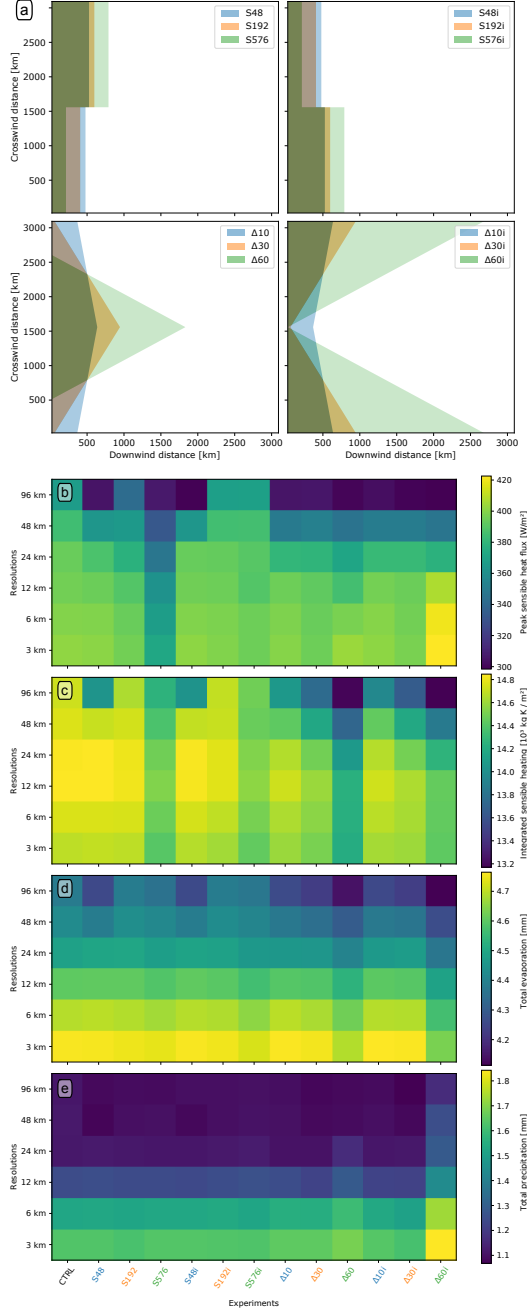


Figure 4. Sensitivity of air-sea heat exchange on both the shape of the marginal ice zone and model grid spacing. (a) Maps of sea ice cover for the different sensitivity experiments. (b-e) Matrices analogous to Fig. 3b-d, but showing the dependence on model grid spacing and the geometry of the sea ice edge.

ization tends to reduce the integral heat and moisture uptake (Fig. 4c,d), although peak fluxes can also be amplified. For example in the narrowest concave triangle ($\Delta 60i$), the peak sensible heat flux is about 5% stronger compared to the straight sea ice edge.

The atmospheric moisture is largely insensitive to the shape of the sea ice edge (Fig. 4d,e). Only in the narrowest triangular shapes ($\Delta 60$, $\Delta 60i$), the moisture cycle is noticeably affected. Here, overall reduced moisture uptake and increased precipitation lead to an overall dryer atmosphere, especially for $\Delta 60i$, where the convergence zone appears to enhance precipitation efficiency.

In summary, air-sea heat exchange is remarkably consistent across all but the most pronounced deviations from a straight ice edge. Thus for most geometries, the distance traveled over open water largely determines the state of the atmospheric boundary layer. This implies that the boundary layer evolution along one stream line is largely independent from the evolution along other stream lines. This is plausible in the absence of mesoscale flow features such as convergence or divergence lines.

A state without mesoscale flow organisation and a perfectly sharp MIZ seems to be the optimal setup for extracting heat from the ocean. In our sensitivity analysis, any deviation from such a state, by smoothing the MIZ or inducing crosswind asymmetries, decreases the overall heat and moisture uptake. At the same time, precipitation remains either about constant (smoothing of the MIZ) or might even increase (triangular edge geometries), leading to an overall dryer atmosphere.

8 Summary and conclusions

We used idealised simulations of a cold-air outbreak using the Polar WRF model to investigate the sensitivity of the air-sea heat exchange on model resolution, sharpness of the marginal ice zone (MIZ), and geometry of the sea ice edge. We characterised differences in the evolution in terms of fetch, the distance traveled over open water. Based on these sensitivity analyses we draw the following conclusions:

1. The *resolved sharpness of the MIZ* strongly affects the peak magnitude of air-sea heat exchange. In particular, peak fluxes are sensitive to the sharpness of the MIZ close to the open ocean. An abrupt end of the MIZ towards the open ocean leads to comparatively high fluxes.
2. *Model resolution* strongly affects the atmospheric water cycle. The higher the model resolution, the smaller the minimum horizontal scale of resolved roll convection, and the smaller the fetch at which roll convection occurs in the simulations. Such roll convection simultaneously increases evaporation and precipitation, leaving the atmospheric moisture budget more or less unchanged across experiments while increasing the atmospheric latent heat uptake. There is no indication that the atmospheric water cycle has converged at our highest resolution with 3 km grid spacing.
3. The *geometry of the sea ice edge* only affects peak and integral heat fluxes when it induces pronounced convergence or divergence zones within the cold air outbreak. Such internal flow asymmetries generally decrease the total heat and moisture uptake within the cold air outbreak, but at the same time generally increase precipitation. Mesoscale flow organization in a cold air outbreak thus results in a dryer boundary layer.

The outlined sensitivities have significant implications for the ocean underlying a modelled cold air outbreak. Higher atmospheric resolution increases both the peak heat fluxes as well as the integral heat transfer from the ocean to the atmosphere. This leads to both a more locally confined destabilisation of the oceanic water column as well as a stronger cooling of the ocean also downstream of the sea ice edge, which is particularly

pronounced in conjunction with an increased sharpness of the MIZ. Thus, models with a higher atmospheric resolution more likely trigger deep ocean convection during cold air outbreaks than models with a coarser grid. This has implications for coupled weather and climate models and sheds light on previously identified model biases near the MIZ related to model resolution. Furthermore, the sensitivity to the sea ice concentration in the MIZ highlights that also internal sea ice dynamics determining the sea ice distribution are key to adequately represent the air-sea heat exchange within and downstream of the MIZ.

Acknowledgments

We thank Annick Terpstra for interesting discussions and providing the basis of the code used to create the WRF initial state and boundary forcing. We thank the National Center for Atmospheric Research (NCAR) for developing and making available the WRF model, and the Polar Meteorology group at the Ohio State University for providing the Polar WRF modifications. We acknowledge internal funding within the Bjerknes Centre for Climate Research to the Atmosphere-Ocean-Ice interaction project (AOI) and the computing resources provided by UNINETT Sigma2 AS.

Data policy. The WRF Model, the Polar WRF modifications, and the code to produce the WRF initial conditions are all publicly available.

References

- Bourassa, M. A., Gille, S. T., Bitz, C., Carlson, D., Cerovecki, I., Clayson, C. A., ... Wick, G. A. (2013). High-latitude ocean and sea ice surface fluxes: Challenges for climate research. *Bulletin of the American Meteorological Society*, 94(3), 403–423. doi: 10.1175/BAMS-D-11-00244.1
- Chen, S.-H., & Sun, W.-Y. (2002). A one-dimensional time dependent cloud model. *Journal of the Meteorological Society of Japan. Ser. II*, 80(1), 99–118. doi: 10.2151/jmsj.80.99
- Chlond, A. (1992). Three-dimensional simulation of cloud street development during a cold air outbreak. *Boundary-Layer Meteorology*, 58(1), 161–200. doi: 10.1007/BF00120757
- Condrón, A., Bigg, G. R., & Renfrew, I. A. (2008). Modeling the impact of polar mesocyclones on ocean circulation. *Journal of Geophysical Research: Oceans*, 113(C10). doi: 10.1029/2007JC004599
- Condrón, A., & Renfrew, I. A. (2013). The impact of polar mesoscale storms on northeast Atlantic Ocean circulation. *Nature Geoscience*, 6(1), 34–37. doi: 10.1038/ngeo1661
- Dickson, R., Lazier, J., Meincke, J., & Rhines, P. (1996). Long-term coordinated changes in the convective activity of the north atlantic. In D. L. T. Anderson & J. Willebrand (Eds.), *Decadal climate variability* (pp. 211–261). Berlin, Heidelberg: Springer Berlin Heidelberg.
- Gebbie, G., & Huybers, P. (2010). Total matrix intercomparison: A method for determining the geometry of water-mass pathways. *Journal of Physical Oceanography*, 40(8), 1710–1728. doi: 10.1175/2010JPO4272.1
- Haarsma, R. J., Roberts, M. J., Vidale, P. L., Senior, C. A., Bellucci, A., Bao, Q., ... von Storch, J.-S. (2016). High resolution model intercomparison project (high-resmip v1.0) for cmip6. *Geoscientific Model Development*, 9(11), 4185–4208. doi: 10.5194/gmd-9-4185-2016
- Hines, K. M., Bromwich, D. H., Bai, L., Bitz, C. M., Powers, J. G., & Manning, K. W. (2015). Sea ice enhancements to Polar WRF. *Monthly Weather Review*, 143(6), 2363–2385. doi: 10.1175/MWR-D-14-00344.1

- Hong, S.-Y., Noh, Y., & Dudhia, J. (2006). A new vertical diffusion package with an explicit treatment of entrainment processes. *Monthly Weather Review*, 134(9), 2318-2341. doi: 10.1175/MWR3199.1
- Inoue, J., & Hori, M. E. (2011). Arctic cyclogenesis at the marginal ice zone: A contributory mechanism for the temperature amplification? *Geophysical Research Letters*, 38(12). Retrieved from <https://doi.org/10.1029/2011GL047696> doi: 10.1029/2011gl047696
- Isachsen, P. E., Drivdal, M., Eastwood, S., Gusdal, Y., Noer, G., & Saetra, O. (2013). Observations of the ocean response to cold air outbreaks and polar lows over the Nordic Seas. *Geophysical Research Letters*, 40(14), 3667-3671. doi: 10.1002/grl.50705
- Jung, T., Serrar, S., & Wang, Q. (2014). The oceanic response to mesoscale atmospheric forcing. *Geophysical Research Letters*, 41(4), 1255-1260. doi: 10.1002/2013GL059040
- Kain, J. S. (2004). The Kain-Fritsch convective parameterization: An update. *Journal of Applied Meteorology*, 43(1), 170-181. doi: 10.1175/1520-0450(2004)043<0170:TKCPAU>2.0.CO;2
- Michel, C., Terpstra, A., & Spengler, T. (2018). Polar mesoscale cyclone climatology for the nordic seas based on era-interim. *Journal of Climate*, 31(6), 2511-2532. doi: 10.1175/JCLI-D-16-0890.1
- Moore, G. W. K., Bromwich, D. H., Wilson, A. B., Renfrew, I., & Bai, L. (2016). Arctic system reanalysis improvements in topographically forced winds near greenland. *Quarterly Journal of the Royal Meteorological Society*, 142(698), 2033-2045. doi: 10.1002/qj.2798
- Müller, G., Brümmer, B., & Alpers, W. (1999). Roll convection within an Arctic cold-air outbreak: Interpretation of in situ aircraft measurements and spaceborne SAR imagery by a three-dimensional atmospheric model. *Monthly Weather Review*, 127(3), 363-380. doi: 10.1175/1520-0493(1999)127<0363:RCWAAC>2.0.CO;2
- Nakanishi, M., & Niino, H. (2006). An improved mellor-yamada level-3 model: Its numerical stability and application to a regional prediction of advection fog. *Boundary-Layer Meteorology*, 119(2), 397-407. doi: 10.1007/s10546-005-9030-8
- Nakanishi, M., & Niino, H. (2009). Development of an improved turbulence closure model for the atmospheric boundary layer. *Journal of the Meteorological Society of Japan. Ser. II*, 87(5), 895-912. doi: 10.2151/jmsj.87.895
- Papritz, L., & Spengler, T. (2017, January). A lagrangian climatology of winter-time cold air outbreaks in the irminger and nordic seas and their role in shaping air-sea heat fluxes. *Journal of Climate*, 30(8), 2717-2737. Retrieved from <https://doi.org/10.1175/JCLI-D-16-0605.1> doi: 10.1175/jcli-d-16-0605.1
- Pickart, R. S., Spall, M. A., Ribergaard, M. H., Moore, G. W. K., & Milliff, R. F. (2003). Deep convection in the irminger sea forced by the greenland tip jet. *Nature*, 424(6945), 152-156. doi: 10.1038/nature01729
- Renfrew, I. A., Pickart, R. S., Våge, K., Moore, G. W. K., Bracegirdle, T. J., Elvidge, A. D., ... Zhou, S. (2019). The iceland greenland seas project. *Bulletin of the American Meteorological Society*, 100(9), 1795-1817. doi: 10.1175/BAMS-D-18-0217.1
- Sein, D. V., Koldunov, N. V., Danilov, S., Sidorenko, D., Wekerle, C., Cabos, W., ... Jung, T. (2018). The relative influence of atmospheric and oceanic model resolution on the circulation of the north atlantic ocean in a coupled climate model. *Journal of Advances in Modeling Earth Systems*, 10(8), 2026-2041. doi: 10.1029/2018MS001327
- Seo, H., & Yang, J. (2013). Dynamical response of the Arctic atmospheric boundary layer process to uncertainties in sea-ice concentration. *Journal of Geophysical Research: Atmospheres*, 118(22), 12,383-12,402. doi: 10.1002/2013JD020312

- 461 Spengler, T., Renfrew, I. A., Terpstra, A., Tjernström, M., Screen, J., Brooks, I. M.,
 462 ... Vihma, T. (2016). High-latitude dynamics of atmosphere–ice–ocean interac-
 463 tions. *Bulletin of the American Meteorological Society*, 97(9), ES179–ES182. doi:
 464 10.1175/BAMS-D-15-00302.1
- 465 Stoll, P. J., Graverson, R. G., Noer, G., & Hodges, K. (2018). An objective global
 466 climatology of polar lows based on reanalysis data. *Quarterly Journal of the Royal
 467 Meteorological Society*, 144(716), 2099–2117. doi: 10.1002/qj.3309
- 468 Strong, C. (2012). Atmospheric influence on Arctic marginal ice zone position
 469 and width in the Atlantic sector, february–april 1979–2010. *Climate Dynamics*,
 470 39(12), 3091–3102. doi: 10.1007/s00382-012-1356-6
- 471 Sukoriansky, S., Galperin, B., & Perov, V. (2005). Application of a new spectral the-
 472 ory of stably stratified turbulence to the atmospheric boundary layer over sea ice.
 473 *Boundary-Layer Meteorology*, 117(2), 231–257. doi: 10.1007/s10546-004-6848-4
- 474 Terpstra, A., Michel, C., & Spengler, T. (2016). Forward and reverse shear environ-
 475 ments during polar low genesis over the northeast atlantic. *Monthly Weather Re-
 476 view*, 144(4), 1341–1354. doi: 10.1175/MWR-D-15-0314.1
- 477 Våge, K., Papritz, L., Håvik, L., Spall, M. A., & Moore, G. W. K. (2018). Ocean
 478 convection linked to the recent ice edge retreat along east greenland. *Nature Com-
 479 munications*, 9(1), 1287. doi: 10.1038/s41467-018-03468-6
- 480 Våge, K., Pickart, R. S., Moore, G. W. K., & Ribergaard, M. H. (2008). Winter
 481 mixed layer development in the central Irminger Sea: The effect of strong, inter-
 482 mittent wind events. *Journal of Physical Oceanography*, 38(3), 541–565. doi:
 483 10.1175/2007JPO3678.1

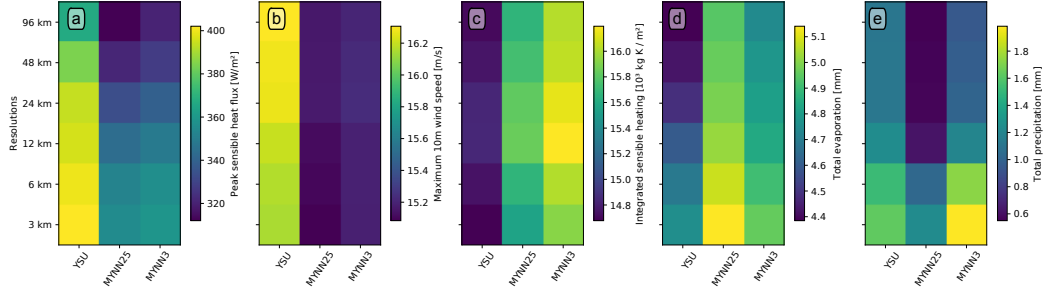


Figure S1. Sensitivity of air-sea interactions on both the boundary layer parametrization and model grid spacing similar to the matrices in Fig. 3b-e. Here, the panels show (a) peak sensible heat fluxes [W m^{-2}], (b) maximum 10-meter wind speed, (c) integrated sensible heating [10^3 kg K m^{-2}], (d) total evaporation [mm], and (e) total precipitation [mm], the latter three all up until a fetch of 1500 km.

Supplement: Sensitivity to the WRF boundary layer parameterisation

We here compare properties of the boundary layer as simulated by (a) the YSU, (b) the MYNN2.5 and (c) the MYNN3 parametrization scheme. We did not include the MYJ or the QNSE scheme, because they produce unphysical discontinuities in the simulated boundary layer properties. For example the latent heat flux decreases by about 30% from one grid cell to the next at a fetch of about 1200 km for most crosswind distances. The discontinuity appears closer to the sea-ice edge with increasing crosswind distances, where the surface pressure becomes increasingly unrealistic compared to real-world cold air outbreaks. It is thus possible that the low surface pressure contributed to exposing this behaviour in the the MYJ and QNSE schemes.

Both MYNN schemes generally simulate lower peak sensible heat fluxes (Fig. S1a), whereas peak latent heat fluxes are largely consistent (not shown). Beyond about 200 km fetch, the sensible heat fluxes are very consistent across all three schemes. The integrated sensible heat uptake is nevertheless considerably higher in the MYNN schemes compared to YSU (Fig. S1c), because the simulated wind speeds over open ocean are considerably lower for the MYNN schemes than for YSU (Fig. S1b). With this reduction in wind speed, the boundary layer has more time to take up heat until it reaches a fetch of 1500 km.

MYNN3 simulates lower latent heat fluxes between about 100 and 600 km fetch (not shown), reducing the integrated moisture uptake (Fig. S1d). MYNN2.5 and YSU simulate very similar latent heat fluxes at all fetches (not shown), but the integrated moisture uptake is larger in MYNN2.5 due to the lower wind speeds (Fig. S1d). Although MYNN3 simulates lower latent heat fluxes, the scheme produces more precipitation (Fig. S1e).

Despite these differences between the schemes, the sensitivity to model grid spacing is fully consistent across the schemes. For all parameters, the boundary layer schemes agree on the grid spacing yielding the highest and lowest value, respectively. Further, the relative increase or decrease between resolutions is comparable across parameterisations. We therefore conclude that the results in this paper remain qualitatively valid irrespective of the chosen boundary layer parametrization.